CHAPTER-4

INFLUENCE OF pH VARIATION ON THE ELECTROCHEMICAL PROPERTIES OF $SrTiO_3$

Uma Sharma, Vani Pawar, and Prabhakar Singh, "Charge particle dynamics and electrochemical behavior of $SrTiO_{3-\delta}$ as anode material for IT-SOFC applications", International Journal of Hydrogen Energy, Pages 1278-1289.

CHAPTER 4: Influence of pH variation on the electrochemical properties of $SrTiO_3$

4.1 Introduction

In chapter 3, it has been studied that with hole substitution, i.e., Sr at La-site, high conductivity of the order of a few S/cm in LTR and more than 10 S/cm in HTR is achieved. Also, between LSF and LSFT, LSF shows the better electrode behavior with high cathodic transfer coefficient. LSF also exhibits maximum ORR compared to LSFT sample. Additionally, in the stability test LSF and LSFT both are stable for more than 72 h long duration in the neutral medium. In the previous chapter, LSFT and LSF exhibited the maximum diffusion coefficient, alongside the completion of catalytic studies across all initial material. Therefore, in this chapter we want to study the electrochemical behavior in strontium titanate ($SrTiO_3$, ST) material, to understand the different catalysis process.

This chapter presents a comprehensive investigation of the charge dynamics in pure strontium titanate. For this purpose, $SrTiO_{3-\delta}$ have been prepared by solid-state reaction route and studied its electrochemical behavior in three various pH media. The scaling behavior of the system has been investigated to understand the conduction mechanism. Further, charge carrier kinetics was also studied to understand the ionic contribution. Electrocatalysis was studied by cyclic voltammetry, confirming the redox process in neutral and basic media, which was further confirmed in the XPS study. The conductivity and catalytic properties of these materials indicated their use in different applications such as in fuel cells, sensors as well as in electrochemical devices.

4.2 Experimental Procedure

$SrTiO_3$ sample was synthesized via the conventional solid-state reaction (SSR) technique. The high-purity precursor Strontium carbonate ($SrCO_3$) and Titanium (IV) oxide (TiO_2) (all from Alpha Aesar with a purity more than 99 %) were added in suitable stoichiometry. These powders were finely ground for 2–3 h using a mortar and pestle and acetone as a mixing medium. Further, powder was dried for 4 h in a hot air oven at 300 ℃ and calcined for 2 h in a muffle furnace at 1200 ℃ in an alumina crucible with a heating rate at 5 ℃ min^{-1}. The calcined powders were now mixed with the PVA binder to reduce the brittleness of the pellet (prepared in the lab; 2.5 g of PVA added to 25 ml distilled water and heated at 80 ℃ using a stirrer) for the pelletization. The circular pellets of 12 mm in diameter and 1.67 mm in thickness at pressure 4–5 N/m^2 were made using a hydraulic press. The obtained pellets were subjected to the sintering process at 1300 ℃ for 2 h at the same heating rate of 5 ℃ min^{-1}. Further, for the study of the electrical properties of the compound, pellets were electroded with platinum paste on both flat surfaces and dried at 750 ℃ for 30 min.

The phase formation of the sintered sample was studied by an X-ray diffraction technique with diffractometer (Rigaku Miniflex-II) using Cu-Kα radiation of wavelength (λ ~ 1.5405 Å) in the range of Bragg's angle 2θ, from 20° to 80° and step size 0.02° at a scanning rate of 1◦/min. Thermogravimetric analysis was performed on ~15 mg sample using Mettler DSC/TGA system at temperatures ranging from RT to 1200 ℃. The microstructure analysis of the sintered pellet was carried out by SEM technique using EVO- Scanning Electron Microscope MA15/18. The electrical measurements were done in the frequency range from 1Hz to 1 MHz and temperature range from 25 ℃ to 700 ℃ , using computer–controlled LCR meter (Wayne

Kerr 6500 P). Fourier transform infrared (FTIR) spectroscopy of the material was carried out in the spectral range of 500–3500 cm^{-1} by using a Nicolet iS5 in the attenuated total reflection (ATR) mode. X-ray photoelectron with $Mg - K\alpha$ beam was used to verify the chemical and oxidation states of the elements.

The electrochemical behavior of the sintered sample was studied by a Keithley 2450 source meter employing three-electrode systems using 1 M Na_2SO_4 neutral medium (pH=7), 1 M KOH basic medium (pH=14), and 0.5 M H_2SO_4 acidic medium (pH=1) as the electrolyte solution. Three electrode systems consisting of Ag/AgCl (KCl saturated) electrode as a reference electrode, Pt wire as counter electrode, and the synthesized sample pellet as a working electrode, were used for CV investigations.

4.3 Results and Discussion

4.3.1 Structural Studies

The XRD pattern of sintered sample is given in Fig. 4.1(a). All the peaks are indexed via JCPDS (card no-350734). The strong XRD peaks at 2θ = 22.52°, 32.14°, 39.88°, 52.34°, 57.51°, 67.59°, 72°, and 77.00° (PDF#350734) were observed. The sample exhibits the cubic crystal structure[166]. Rietveld refinement has been done with the help of FULLPROF Suite software with the Pseudo-Voigt wave function that gives the best fit (χ^2) value. The lattice parameter is obtained as 3.9084 Å. The other fitting parameters are found as χ^2~8.01, R_p and R_{wp} are 12.7 and 13.7, respectively. The atomic positions and other parameters are mentioned, in Table 4.1.

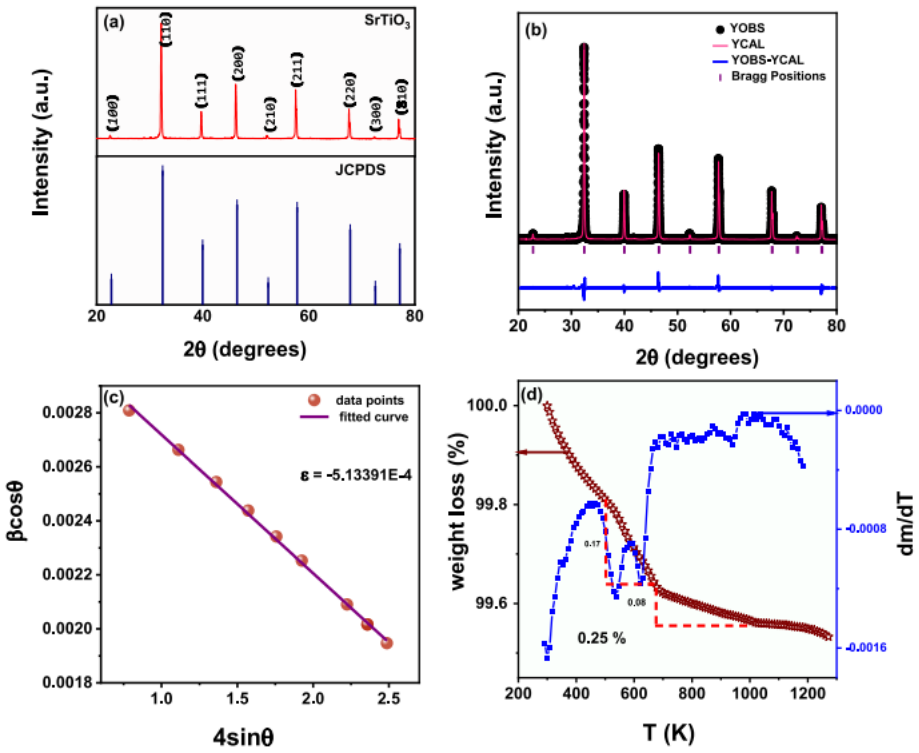

Figure 4.1 (a) Powder X-ray Diffraction of sintered $SrTiO_3$ sample with JCPDS (350734) **(b)** Rietveld refinement of $SrTiO_3$ **(c)** W–H plot of $SrTiO_3$ **(d)** TGA curve of weight loss and the mass change with temperature $SrTiO_3$.

The micro strain and the crystallite size were calculated with the help of the Williamson-Hall (W–H) plot (refer to Fig. 4.1(c)) using equation-

$$\beta cos\theta = 4\varepsilon sin\theta + \frac{K\lambda}{D} \tag{4.1}$$

where D is average crystallite size, ε is microstrain, β is full-width half maxima (FWHM) at Bragg's angle (2θ) and λ is X-ray wavelength of Cu-Kα (1.54 Å) and value of Scherrer's constant (K) is 0.94[167]. The crystallite size value estimated from the W-H plot is 430 nm and the nature of the strain is compressive [168].

Table 4.1 Parameters obtained from the refinement.

	Atomic positions and occupancy obtained from refinement				
Elements	**Wyckoff Positions**				
	X	Y	Z	B	Occupancy
Sr	0.5000	0.5000	0.5000	0.24126	0.97249
Ti	0.0000	0.0000	0.0000	0.16943	0.98678
O	0.5000	0.0000	0.0000	1.21230	2.89675

For the thermal stability of $SrTiO_3$, TGA measurements of the calcined powder was performed and the corresponding data are shown in Fig. 4.1(d). The weight loss in the temperature range 200–1400 K is observed to be 0.25 %. Two significant exothermic peaks are observed in the temperature derivative curve at about 567 K and another at 662 K corresponding to the weight loss in TGA first at ~480 K and then at 680 K steadily, which can be attributed to the O_2 and CO_2 loss, respectively[169]. Here, the oxygen deficiency, δ = 0.3 from the TGA curves after 600 K has been estimated[169]. A partial Schottky defect is reported in the $SrTiO_3$ system[170]. Kröger -Vink notation are used to write the defect equation in $SrTiO_3$ –

$$2SrCO_3 + 2TiO_2 = 2SrTiO_3 + 2CO_2 \quad (4.2)$$

$$Sr_{Sr} + Ti_{Ti} + 3O_o \rightleftharpoons V''_{Sr} + V''''_{Ti} + 3V_o^{\cdot\cdot} \quad (4.3)$$

Fig. 4.2 depicts the sintered pellet's SEM micrographs at room temperature; the grains are uniformly distributed over the sample's surface. The compound's average grain size estimated with the help of Image J software is found to be 810 nm with a porous structure.

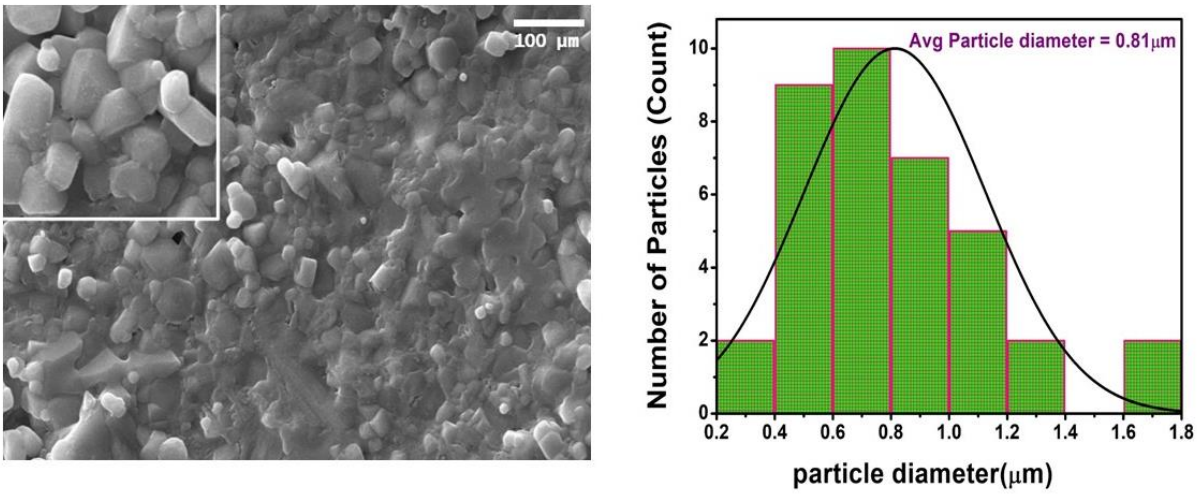

Figure 4.2 Inset shows the zoomed -in version of SEM micrograph of the sintered pellet and particle size calculation histogram.

4.3.2 Electrical and Impedance Studies

For the sample $SrTiO_3$, the variation of $log\sigma$ vs $logv$ in the temperature range 500 °C to 700 ℃ is depicted in Fig. 4.3(a). Jonscher Power law describes frequency dependent conductivity of the studied sample by equation below [171].

$$\sigma' = \sigma_{dc} + Av^{\eta} = \sigma_{dc}[1 + \frac{Av^{\eta}}{\sigma_{dc}}] = \sigma_{dc}\ [1 + (\nu/\nu_h)^{\eta}\,, \tag{4.4}$$

where $$\nu_h = \left[\frac{\sigma_{dc}}{A}\right]^{1/\eta}$$

where σ_{dc} is the DC conductivity, ν is the frequency of the applied electric field, A is a constant, ν_h is the hopping frequency, and η is the exponent factor that measures the extent of ion interaction with the lattice [172]. In Fig. 4.3(a) the conductivity is frequency independent at lower frequencies and frequency dependent at higher frequencies. Conductivity spectra

exhibit dispersion at high frequency representing unsuccessful hopping of charge carriers [173].

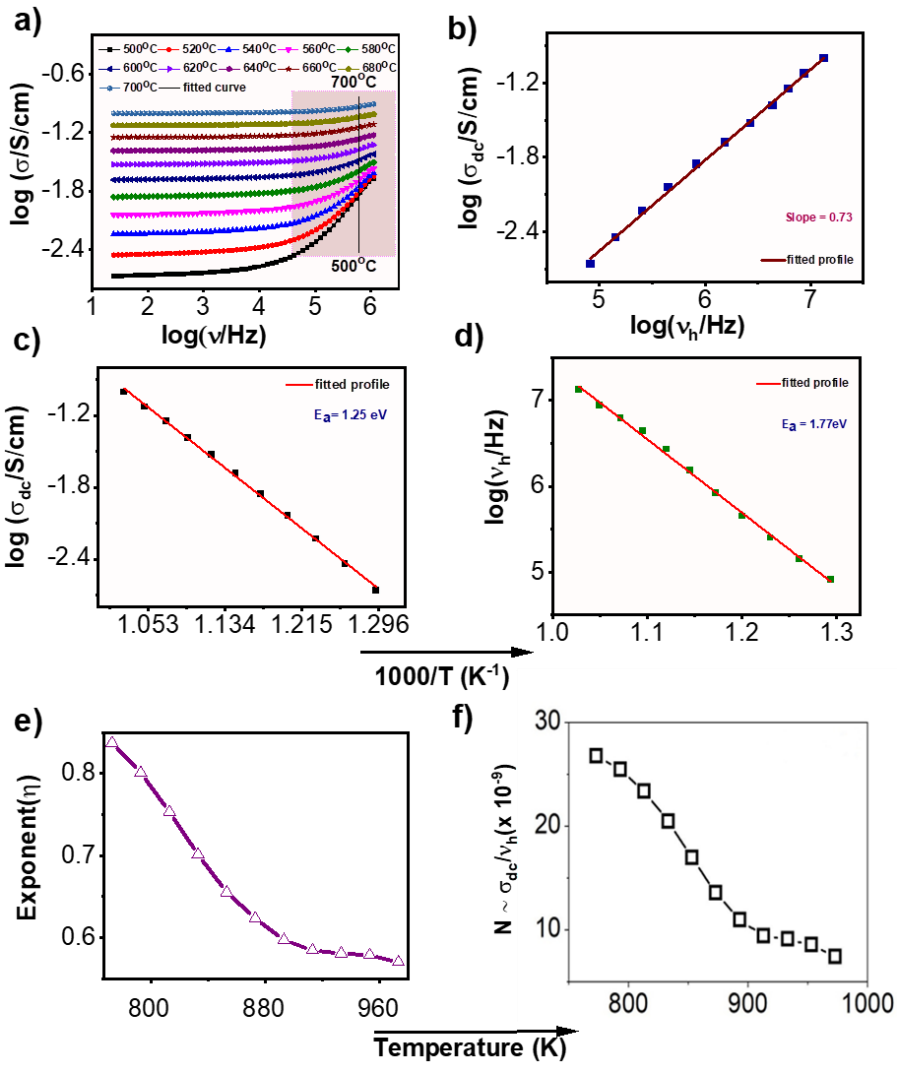

Figure 4.3 (a) Variation of *logσ* vs *logv* at various temperatures **(b)** $log\boldsymbol{\sigma_{dc}}$vs $log\boldsymbol{\nu_h}$**(c)** $log\boldsymbol{\sigma_{dc}}$ vs 1000/T **(d)** $log\boldsymbol{\nu_h}$vs 1000/T for activation energy **(e)** variation of exponent with temperature and **(f)** charge carrier concentration with temperature.

The parameters σ_{dc} , ν_h , and η are calculated by fitting the conductivity spectra (Fig. 4.3(a)) with Jonscher Power Law (eq. 4.4) between the temperature range 500 ℃ to 700 ℃. In the Arrhenius representation, Fig. 4.3(c),(d) for the bulk conductivity and the hopping frequency

the calculated activation energy E_a is obtained as 1.25 eV and 1.77 eV, respectively. This indicates that the oxide ions are participating in the conduction process. In plot $log\sigma_{dc}$ vs $log\nu_h$, in Fig. 4.3(b), the slope value is nearly 0.73, this indicates that conductivity is governed by hopping [172].

Fig. 4.3(e) describes the temperature vs exponent 'η' which is related to the degree of correlation among moving ions [172]. As the temperature increases the exponent decreases. This indicates that with increasing temperature the degree of correlation among moving ions decreases. Charge carrier concentration factor *N* has been calculated with help of Almond-West formalism [174]. Here *N* is proportional to $\sigma_{dc}\ /\nu_h$, where σ_{dc} is the DC conductivity and ν_h is the hopping frequency, refer Fig. 4.3(f). The observed behaviour of carrier concentration *N* with temperature shows an increment which is quite similar to exponent 'η' (Fig. 4.3(e)). These variations of the exponent and charge carrier concentration factor with the temperature [175]. The ion dynamics and charge hopping correlation are dependent on the carrier concentration and temperature.

In Fig. 4.4(a) Nyquist plots (cole-cole plot) for the ST is shown in the temperature range 400℃ to 575 ℃ and in the frequency range 20Hz to 10MHz. Each semi-circular arc in the impedance profile has its own characteristics. Generally, they exhibit three semi-circular arcs: one in the high-frequency region (a minor arc intersecting at the origin), another in the mid-frequency region, and a third one in the low-frequency region as shown in Fig. 4.4(a).

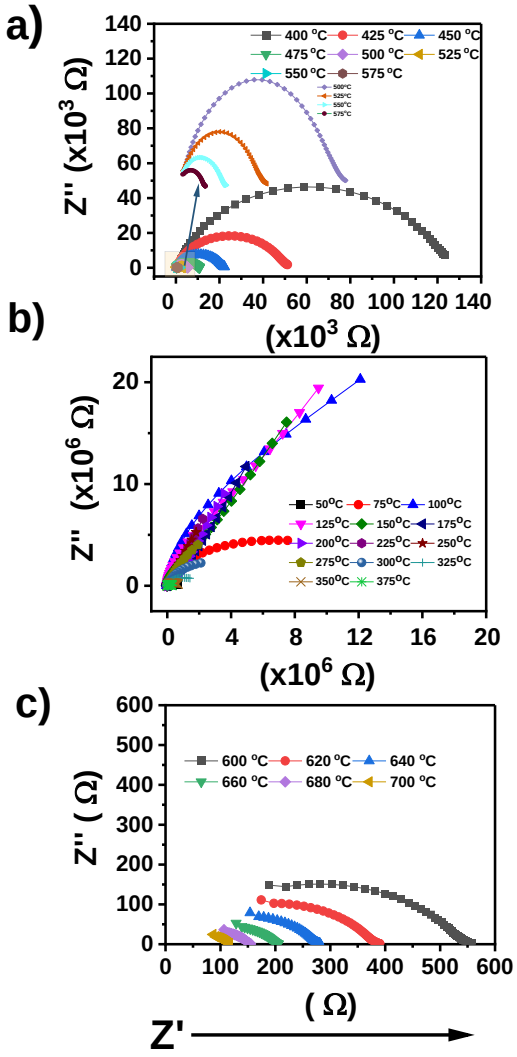

Figure 4.4 (a) Nyquist Plot from 400 ℃ to 575 ℃ **(b)** at low temperature (50 ℃ to 375 ℃) **(c)** at high temperatures (600 ℃ to 700 ℃) imaginary part of $\boldsymbol{Z}$ vs real component of $\boldsymbol{Z}$.

In high frequency region the data are enlarged and indicated in Fig. 4.4(a) representing the bulk conductivity (grain conductivity). These are related to the specific relaxation frequency (ω_{max}) and mathematically expressed as $\omega_{max} = 1/t$, here 't' is relaxation time depending only on the fundamental properties i.e., grain interiors or bulk, grain boundaries, etc, of the materials. Also, the real axis explains the involvement of grains and grain boundaries in these three different frequency regions with the help of intercepts obtained from these arcs. In this

case, the arcs are more distinct with the rise in the frequency and the temperature range of 400 ℃ −575 ℃. Further, there is one semi-circular arc in the temperatures 400 ℃ to 575 ℃ which confirms the bulk contribution whereas for the temperature above 575 ℃ we observed only one spike, and for the temperature less than 400 ℃, these arcs corresponding to grain contribution disappeared, Fig. 4.4. (b)-(c).

Fig. 4.5(a) is representation of a real part of impedance (Z') with frequency at different temperatures. The figure indicates that with increasing frequency the impedance decreases. It suggests that conduction is increasing with the frequency and temperature which is because of forward backward correlated hopping of the charge particle [176].

Fig. 4.5(b) represents the variation of imaginary part of impedance (Z'') with frequency within the temperature range of 300 ℃ to 700 ℃. Here, it is clearly shown that there is a peak after 300 ℃ and with the increase in temperature the peaks shift towards a higher frequency and disappear after 600 ℃. This behaviour shows that system exhibits the temperature-dependent relaxation [177] and relates the existence of static species at lower temperatures and defects at high temperatures [176].

Fig. 4.5(d) shows the cole-cole plot at 500 ℃. The data is fitted using ZSimpWin software. The equivalent circuit consisting of one resistance and two parallel $R - Q$ circuit connected in series is shown in the same Fig. 4.5(d), where R is resistance and Q is the constant phase element (CPE) which implies the occurrence of multiple relaxations processes. The constant phase element has the properties of capacitance and resistance. Mathematically it can be written as –

$$Q_{CPE} = \frac{1}{Y_o\,(j\omega)^K}; \quad 0 \leq K \leq 1 \tag{4.6}$$

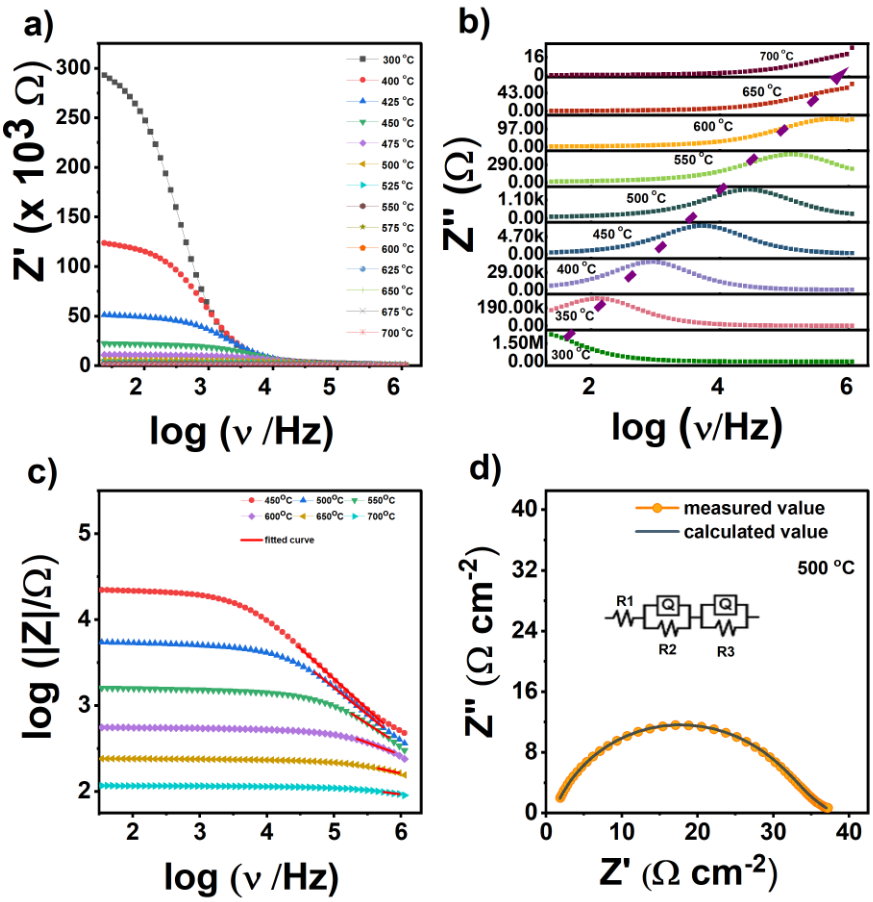

Figure 4.5 Frequency dependence of **(a)** real part of $\boldsymbol{Z}$ **(b)** imaginary part of $\boldsymbol{Z}$ **(c)** modulus of $\boldsymbol{Z}$ **(d)** Nyquist plot with the equivalent circuit at 500 ℃.

here 'K' quotes the variance from ideal capacitive behaviour [177]. It gives one and zero values for pure capacitive and pure resistive cases, respectively.

Ghosh Scaling uses hopping frequency as the scaling parameter and with the help of this, conductivity spectra have been scaled. The scaling mechanism is described by the equation-

$$\frac{\sigma'(\nu)}{\sigma_{dc}} = F\left(\frac{\nu}{\nu_h}\right), \tag{4.7}$$

where σ_{dc} is the dc conductivity, ν_h is the hopping frequency and F is the temperature-independent function [175]. As a consequence of the TTSP (time-temperature superposition

principle) , these conductivity isotherms values can be superimposed on a single master curve by utilizing conductivity and hopping frequency as the scaling parameter [178] as shown in Fig. 4.6 .

The Ghosh scaling phenomenon is observable within the temperature range of 500 ℃ to 700 ℃. Within this temperature range, conduction remains unaffected by both frequency and temperature. This phenomenon is associated with the variance in the quantity of charge carriers due to temperature fluctuations, while the underlying conduction mechanism remains consistent [179].

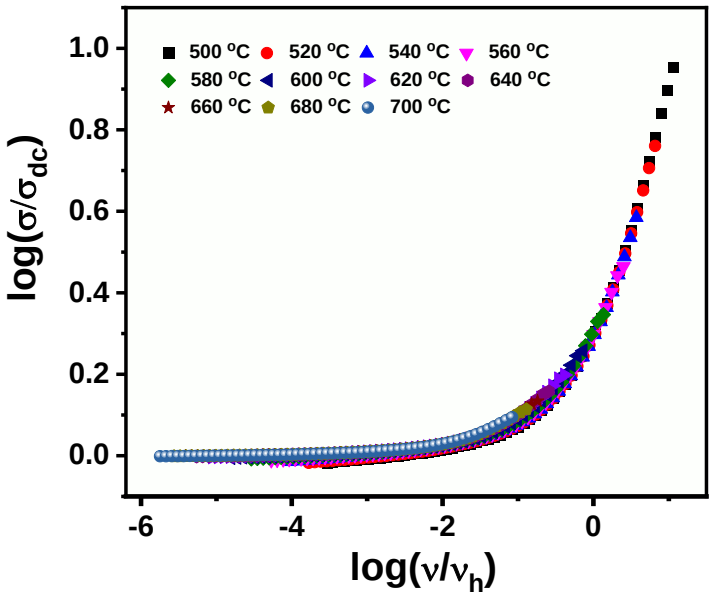

Figure 4.6 Ghosh scaling of $SrTiO_3$.

To get a clear understanding of various charge transport processes in an ion conductor, only impedance analysis is not sufficient. Modulus spectroscopy of the prepared sample is analysed to study the electrical transport process and ion dynamics with frequency and temperature. Here, Fig. 4.7(a) illustrates the frequency dependence of the imaginary part of the modulus at

different temperature. It shows the change in the peak maxima position with frequency and temperatures. This reflects the motion of the ions in the material. The conduction process and the relaxation process are related to the lower and the higher frequency side of the peak which allows the ions to move within their boundaries [180][181].

There is a short-range motion for the charge carriers above the peak frequency region and they are mobile over a long range below the peak frequency region. Here, we observe a peak shift toward the higher frequencies with the temperature rise. Movement of charge carriers enhanced due to this increased relaxation time suggesting the Debye–type relaxation is not followed [180]. This implies the possibility of both the short-range (localized) and the long-range (non-localized) mobility of the charge carriers.

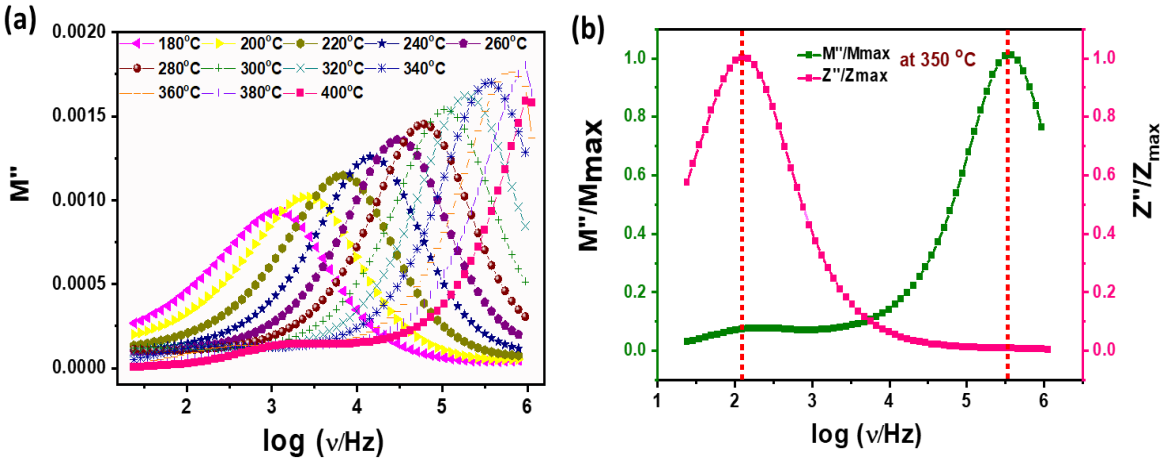

Figure 4.7 (a) Electric modulus spectra of $SrTiO_3$ at various temperature **(b)** frequency variation of Electric Modulus $\boldsymbol{M''/M''_{max}}$ and impedance $\boldsymbol{Z''/Z''_{max}}$ at 350 ℃

In Fig. 4.7(b), we plot the normalized value of the imaginary part of modulus (M'') and impedance (Z'') at a temperature of 350 ℃ to study the movements of the different types of charge carriers. A non-local movement of the charge carriers is associated with the peak overlap, whereas peak separation is associated with the localized and non-localized motions.

Here, we observe a clear separation of the peak of M'' and Z'' which is confirming the presence of both kinds of the charge carriers [182].

4.3.3 Electrochemical properties

Cyclic voltammetry (CV) measurements in three media, viz. neutral, basic, and acidic were performed and plots between current density and potential are shown in Fig. (4.8) at different scan rates in the potential range -1.5 V to +1.5 V.

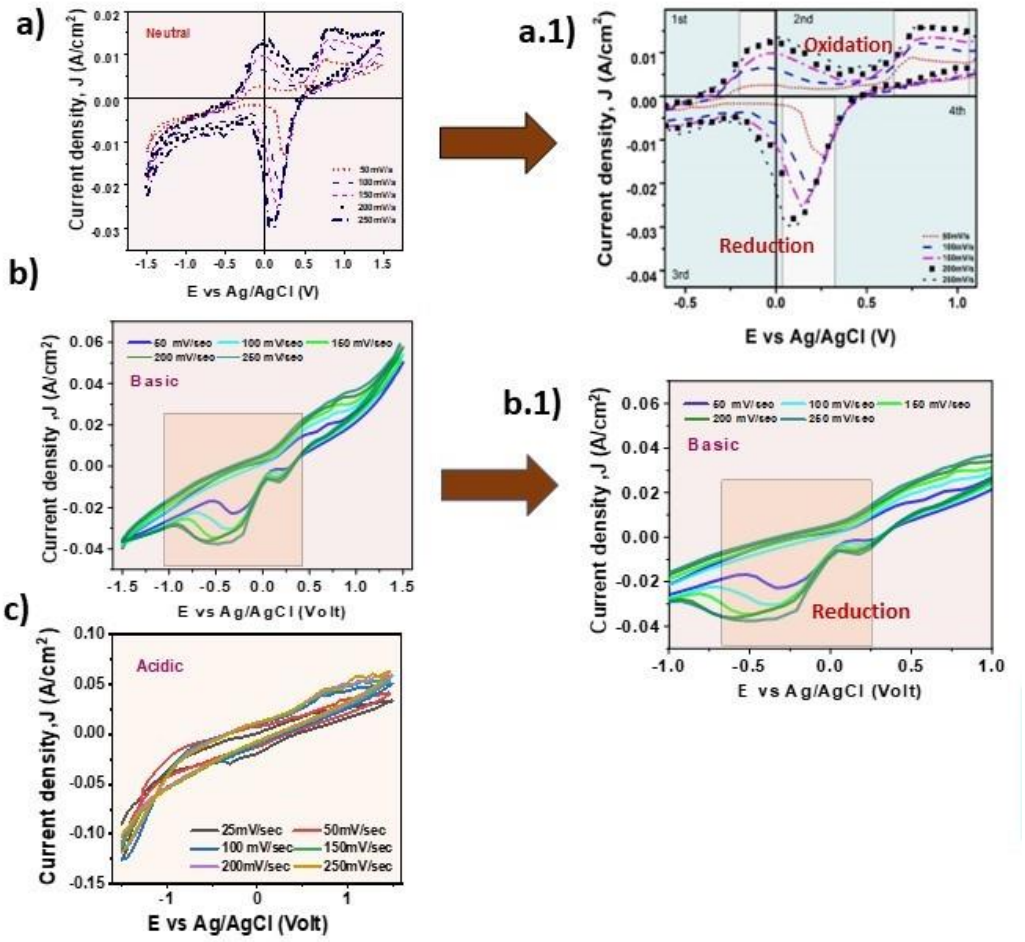

Figure 4.8 Cyclic voltammograms of $SrTiO_3$ at **(a)** neutral **(b)** basic **(c)** acidic medium and peaks of oxidation and reduction in **(a.1)** neutral medium **(b.1)** basic medium.

Here, in Fig. 4.8(a) of CV curve of neutral medium, the first cycle is quite different from the second and third cycles in both the anodic and cathodic subdivisions. Also, we observe that there is one reduction peak in the cathodic region and two oxidation peaks in the anodic region. These other kinks of oxidation peak may be because of the excess oxygen intercalation into the structure [183]. But in the case of basic medium Fig. 4.8(b), we observe reduction peak is more favourable than oxidation peak whereas in the case of acidic medium there is no any prominent peaks of oxidation and reduction appeared. This may be because it forms a thin layer of oxides on its surface of TiO_2 which passivate the material and prevent to form any reaction. Since, the measurements in the acidic medium does not give any relevant information, therefore we dropped the CV measurement in acidic medium and consider here onward the cases of measurements in neutral and basic media only. It is clear from Fig. 4.8(a)-(b) that an increase in the area under the curve is observed with the scan rate and a corresponding rise in the peak current density is noticed. This phenomenon exhibits fast ionic and electronic transport rates due to the shrinkage of the diffusion layer [184].

The reversibility, quasi-reversibility or irreversibility of an electrochemical process is related to the charge transfer kinetics taking place at the working electrode. There exists a correlation between the peak-to-peak separation, which represents the difference between the anodic and cathodic peaks (ΔE_p), and the degree of reversibility [158]. Here in the neutral medium cyclic voltammogram, ΔE_p, ΔE_p calculated from the difference of anodic peak and cathodic peak (Fig. 4.8(a)) is less than 57 mV, indicating a rapid electrochemical reaction and a reversible system. But, in basic system (Fig. 4.8(b)) the value of (ΔE_p), is higher than 57 mV and for the higher scan rate, the oxidation peak does not appear, which indicates the presence of an irreversible system would be present in the basic medium [158]. To obtain more assessment of

reversibility/irreversibility the half peak potential ($E_{p/2}$) and inflection point (E_i) values are calculated from the first and second derivative of the cyclic voltammogram as shown in Fig. 4.9(a) [185]. These values are plotted in Fig. 4.9(b) and it indicates that the value of $E_{p/2}$ and E_i is nearly overlapped in the case of the neutral medium, however in the case of basic medium these values do not overlap. This suggests that our system is reversible in the neutral medium but not in the case of basic medium. This also indicates that with the pH variation, system transforms from reversible to irreversible nature.

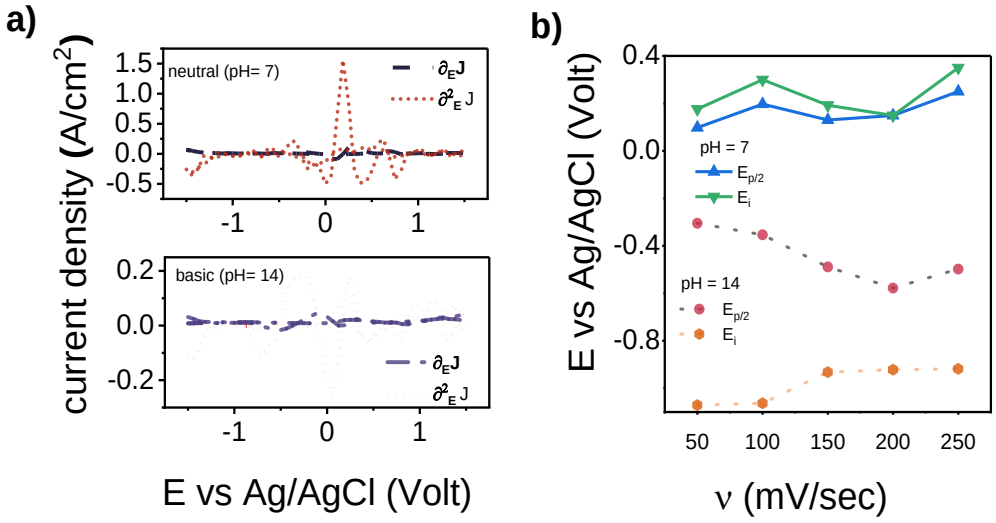

Figure 4.9 (a) First and second derivative at the scan rate 100mV/sec **(b)** $E_{p/2}$ and E_i with the scan rate.

In addition, the CV study in both the neutral and basic media indicates that despite the oxygen evolution regime (OER), the oxygen reduction regime (ORR) has a larger area under the curve because these activities are related to these oxidation and reduction paths. The careful observation reveals that in the neutral medium Fig. 4.8(a) a subsequent cycle exhibits two oxidation peaks in two different quadrants which may be due to the other multiple oxidation processes occurring. In basic medium Fig. 4.8(b), two reduction peaks are observed. From

these curves, it is noticed that the peak intensities of both the cycles are not that much different from each other which reveals the activation process during the charging process.

Since, in an electrode the double layer region where there is no any faradic reaction, the current flows across the electrochemical interface depending on the scan rate according to equation [186]-

$$I = a.\upsilon^{b} \tag{4.8}$$

where 'I' is the current flow across the electrochemical surface and 'υ' is the scan rate and 'b' is the exponent factor, Fig. 4.10(a). The value of $b \sim 1$ shows the capacitive process and for less than value 1, the diffusion of oxide ion is dominant [187].

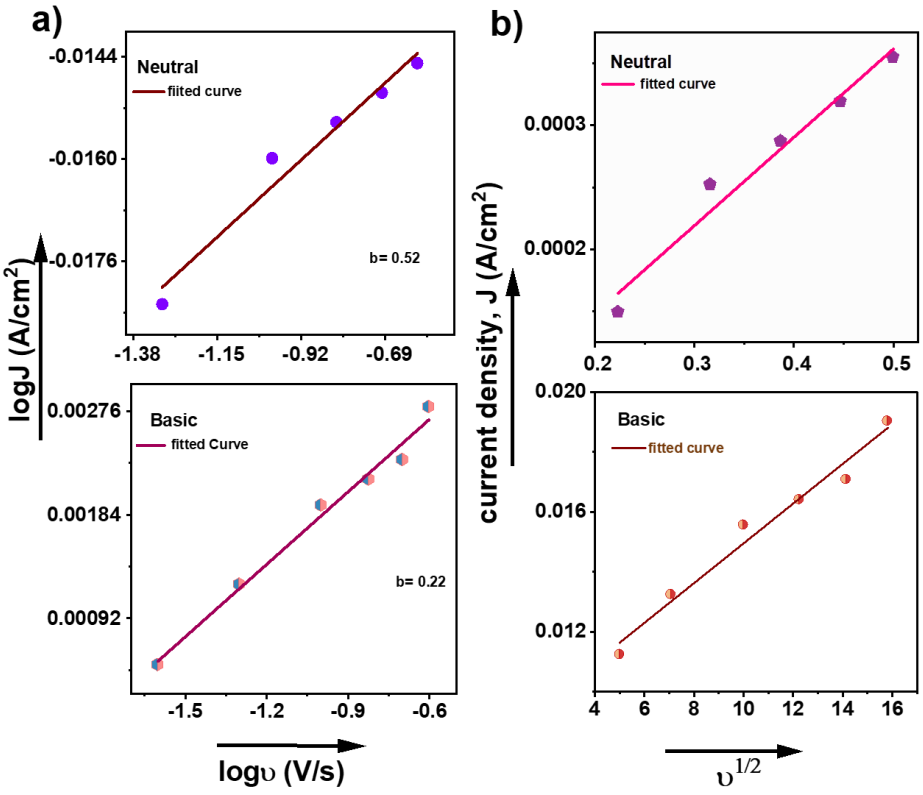

Figure 4.10 Variation of **(a)** *logj* vs $log\upsilon$ **(b)** current density with scan rate $\boldsymbol{\upsilon^{1/2}}$

Here, in Fig. 4.10(a) the value of 'b' from the plot of $logj$ and $logv$ is near 0.52 for neutral medium and 0.22 for the basic medium which shows the diffusion of oxide ion is more prominent in basic medium. This behaviour is favourable in energy storage mechanism and the current response could be explained by the ion diffusion-limited electron intercalation or de-intercalation mechanism suggesting the system could behave like a pseudo capacitor [158]. Further, in Fig. 4.10(b), we observe a linear variation in the peak current with $v^{1/2}$ which elucidates the diffusion mechanism [188].

Fig. 4.11(a) and (b), show a current response with time for 4000 s at the fixed potential 2V for both the media. These figures show a small disturbance initially but after that, it is stable for a given time. The current-time response is fitted with the exponential decay and transient decay time is obtained for both the media. A clear observation emerged that the transient decay time is longer in neutral medium compared to a basic medium indicates that neutral medium persists a better current time dependency for the diffusion-controlled process occurring at the working electrode in comparison to the basic medium [189].

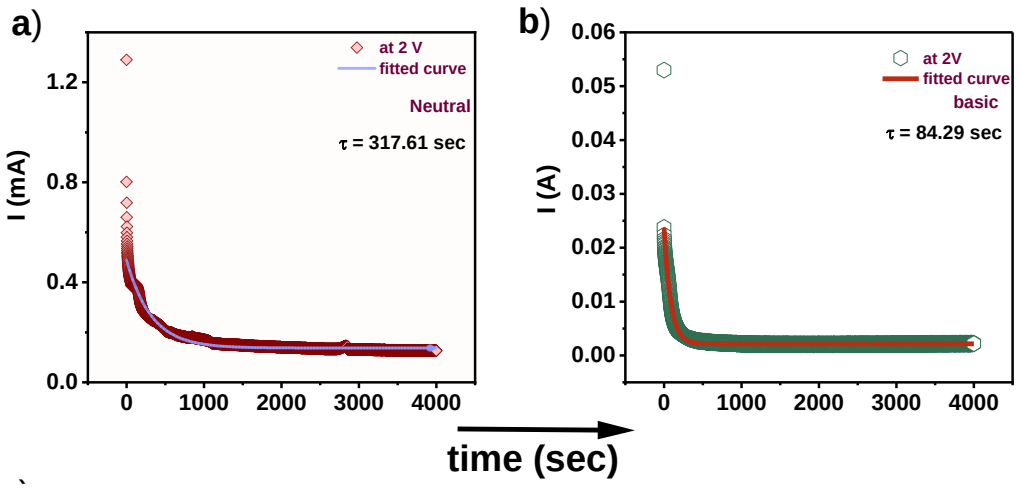

Figure 4.11 Current-time response at 2V **(a)** neutral medium **(b)** basic medium.

4.3.4 FTIR Analysis

To understand the formation of oxide band groups and hydroxyl band groups, FTIR spectra of ST sample were measured. In Fig. 4.12 the FTIR spectra are shown post CV measurements in the spectral range 500-3200 cm^{-1}, in the neutral, basic and acidic media. For the comparison purpose, the FTIR spectra before CV is also shown. A broad absorption band for the $SrTiO_3$ system is observed. The peaks at 510 cm^{-1} and 625 cm^{-1} are related to the TiO_6 octahedron bending and stretching vibrations, respectively [190].

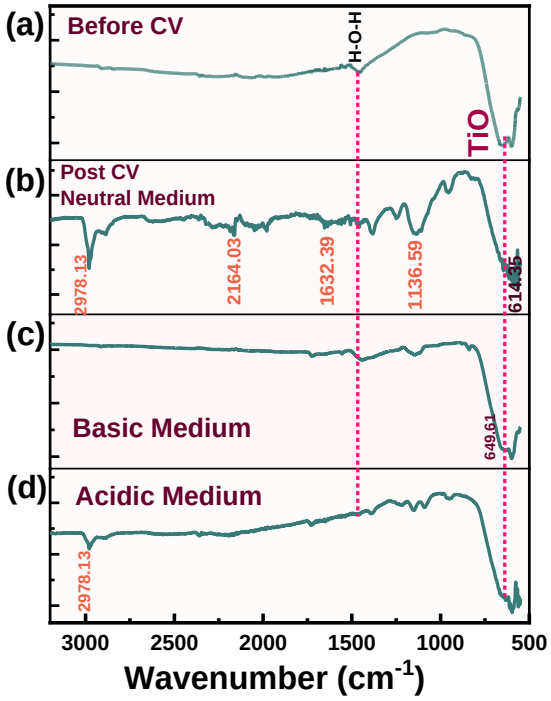

Figure 4.12 FTIR spectra of $SrTiO_3$.

There is an absorption peak at around 1500 cm^{-1} which may be assigned to the bending vibration of H-O-H from the adsorbed H_2O that is significant in the neutral and basic media. In the post CV spectra Fig. 4.12 (b) and (c), peaks of Na_2SO_4 and KOH with the characteristic peaks of $SrTiO_3$ around the broad-spectrum 500 cm^{-1} to 620 cm^{-1} are observed. These

absorption peaks are in consistent with the literature [191]. An overlay of the vibration peaks of TiO and SO_4 at around 614 cm^{-1} in the post CV spectra of neutral medium are also detected. In basic medium a broad-spectrum peak of KOH with the peak of TiO at around 500 cm^{-1} to 650 cm^{-1} due to the K-O bond stretching vibrations are observed [192]. But no any such specific peak is observed in the acidic medium. The results demonstrate that Ti is participating in the redox process with the Na_2SO_4 and KOH.

4.3.5 XPS Analysis

Figure 4.13(a) gives the complete spectra of XPS and shows the energy levels of the elements Sr, Ti, and O in the strontium titanate. Due to the contaminating hydrocarbon species on the specimen surface, the binding energy of the C1s peak (284.7 eV) is used as a reference for the correction. The presence of ionic bond in between the Sr, Ti, and O atom is confirmed by the binding energy observed in XPS spectrum. Figure (4.13(b-d)) illustrates the core-level XPS spectra of Sr-3d, O-1s, and Ti-2p, obtained after deconvoluted elemental spectra. Sr-3d map (Fig. 4.13(c)) , which shows two pairs of peaks at 132.8 eV and 135.5 eV is related to the Sr–O bond and other peaks at 134.68eV and 135.5 eV are related to $SrCO_3$ bond facilitating the reaction Sr with O_2 and CO_2 [193]. The deconvolution of Ti 2p spectra in (Fig. 4.13(d)) gives two peaks at 463.91 eV and 458.15 eV with the satellite peak at 472.50 eV, which is consistent with the database results. Since Ti has multiple oxidation states in which the peak at 458.15 eV corresponds to the Ti^{4+} with the possibility of presence of Ti^{3+} / Ti^{2+} at the peak of 463.91 eV [169]. The satellite peak may be the result of the Ti's d orbital and O's p orbital interaction which may be attributed to metal-ligand interaction [169].

In the O-1s core level (Fig. 4.13(b)), XPS spectra are fitted with the four peaks with binding energies of approximately 527.87 eV, 529.27 eV, 531.33 eV, and 531.63 eV corresponding to the O=C–O bond, metallic bond (Bi-O, Ti-O, Na-O), hydroxide bond, and chemically adsorbed oxygen on the surface O_{chem}, respectively.

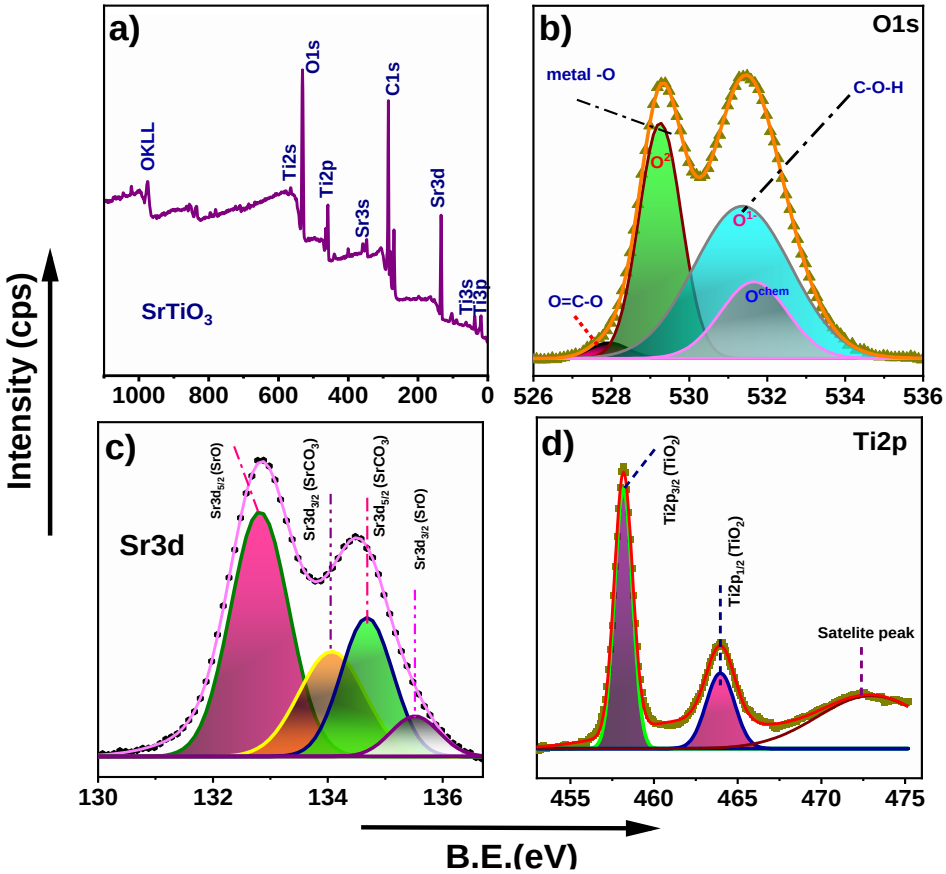

Figure 4.13 X-ray photoelectron spectroscopy measurements (de-convoluted peaks) of $SrTiO_3$ **(a)** the wide spectra **(b)** O1s spectra **(c)** Sr3d spectra **(d)** Ti2p spectra.

The Metal-O peak signifies the presence of an oxygen vacancy, while the metal -hydroxide peak indicates the adsorption of a vacancy [188]. Furthermore, a stronger intensity of the Metal-O peak relative to the other two peaks in the spectrum is also observed, suggesting a

substantial presence of oxygen vacancy defects (V_o) [194].The oxygen vacancies are generated as per the following equation -

$$2TiO_2 \rightarrow 2Ti'_{Ti} + V_o^{\cdot\cdot} + 3O_o + 1/2O_2 \quad (4.9)$$

According to the Dupin et al [195] interpretation, the lower and intermediate one are related to BE peak corresponding to O^{2-} ions and O^{1-} ions, respectively, whereas the higher BE peak is indicative of surface adsorbed oxygen, O_{chem} [196]. The relationship between the peak areas corresponding to metal-oxygen and metal hydroxide directly corresponds to the concentration of oxygen vacancies and the calculated value from the O1s spectrum which is found to be approximately 0.67 [169]. We calculated the average valence value of oxygen anions (V_{alo}) in the sample with the help of area ratio and can be given by the equation-

$$V_{\text{alo}} = -1.00 - I_{\text{A}} , \quad (4.10)$$

where I_A is obtained from the ratio of metal-oxygen and metal hydroxide peak area.

The average valence value is found to be 1.67 which is considerably high. This high oxidative ion O^{2-}/O^{1-} formation provides better electrochemical activity because more active species would be present for the catalysis of the redox process [162]. Also this is favourable for the OER performance [197]. The result is consistent with the CV process and corroborate with our $SrTiO_3$ electrochemical performance. Moreover, the earlier report confirms that, transition metal ions Ti^{4+} form a covalent bond with the O^{2-}which is consistent with the above discussion regarding good redox catalytic activity [198]. The intensity of the oxidation of the adsorbed oxygen ion depends on collectively with the covalence of the oxygen-transition metal bonds in perovskites as well as the hybridization between the transition metal's 3d electron orbitals and oxygen 2p electron orbitals [198], which is confirmed through the XPS studies.

This also plays a critical role in electrochemical reversibility resulting more electron transfer in the electrolysis processes [193].

Since the nominal Sr interaction is observed in strontium s- orbitals and oxygen's s-orbitals and p-orbitals [199] therefore from the above discussion we can say that Ti participates in both the oxygen intercalation process and the faradaic surface redox process for the significant use in energy storage applications [193].

4.4 Conclusion

In this work, the charge dynamics of the $SrTiO_3$ is investigated. A collective electric and modulus studies show that the reason of relaxation process and conduction mechanism is the double ionization of oxygen vacancies. The system follows Ghosh scaling, indicating that the hopping frequency makes a suitable scaling parameter. The electrochemical studies in different media suggests a high involvement in the catalytic activity as the multiple oxidation states tend to the OER mechanism in the neutral medium but not significant in other two i.e., basic and acidic media. The high reduction regime in the cathode region shows that the ORR mechanism may take place in neutral and basic media but not in the acidic medium. The redox process and the transition metal Ti^{4+} take part in the redox reaction due to its multiple oxidation states and good catalytic activities.